

Effect of Aging Treatment on the Microstructure and Resistivity of a Nickel-Base Superalloy

RICKY L. WHELCHER, V. SIVA KUMAR G. KELEKANJERI,
ROSARIO A. GERHARDT, and JAN ILAVSKY

The γ' precipitation behavior of age-hardened Waspaloy, aged at 998 K, 1073 K, and 1148 K (725 °C, 800 °C, and 875 °C) for times ranging from 0.5 to 263.5 hours, were evaluated *via* analysis of ultra small angle X-ray scattering (USAXS) curves and scanning electron microscopy (SEM) micrographs. The USAXS spectra revealed a single precipitate size distribution at the earliest aging times, which evolves into a bimodal precipitate size distribution at later aging times. The primary precipitate radius displayed $t^{1/3}$ coarsening dependence for aging at 1073 K and 1148 K (800 °C and 875 °C); however, the primary radius increased with $t^{0.4}$ dependence at 998 K (725 °C), most likely due to mixed growth and coarsening. A figure of merit, η' , consisting of two terms, one associated with precipitate size and volume fraction and the other with compositional fluctuations, was proposed. η' shows direct empirical correlations with changes in the measured electrical resistivity.

DOI: 10.1007/s11661-010-0483-0

© The Minerals, Metals & Materials Society and ASM International 2010

I. INTRODUCTION

Waspaloy* is a precipitation-hardenable nickel-

*Waspaloy is a trademark of United Technology Corp., Hartford, CT.

base superalloy used in hot-section components of land and air-based gas turbine engines. Superalloys are ideal for this application due to these materials' high-temperature strength, creep resistance, and corrosion resistance. The exceptional mechanical properties inherent to in-service superalloy components are obtained as a result of the formation of nanometer-sized precipitate phases (γ') within a matrix phase (γ) through proper heat treatments. These precipitates greatly impede dislocation motion under an applied stress. However, the ability of these precipitates to impede dislocations will vary with precipitate size, spacing, and volume fraction.^[1] Since gas turbine engine components operate at elevated temperature, the heat-treated precipitate microstructure will evolve with in-service extended thermal exposure, thereby altering the mechanical properties of the alloy. Therefore, developing a methodology that will allow nondestructive evaluation of the microstructural evolution in superalloys is desirable in order to track the mechanical properties of gas turbine engine components throughout their service lifetime.

RICKY L. WHELCHER and V. SIVA KUMAR G. KELEKANJERI, Graduate Research Assistants, and ROSARIO A. GERHARDT, Professor, are with the School of Materials Science and Engineering, Georgia Institute of Technology, Atlanta, GA, 30332. Contact e-mail: rosario.gerhardt@mse.gatech.edu JAN ILAVSKY, Scientist, is with the X-ray Operations Division, Argonne National Laboratory, Argonne, IL 60439.

Manuscript submitted February 8, 2010.

Article published online December 9, 2010

Small angle scattering (SAS) techniques, such as small angle neutron scattering and small angle X-ray scattering (SAXS), have been shown to yield promising results for obtaining microstructural information in superalloys.^[2-8] Since the precipitate microstructure ultimately determines the mechanical properties of superalloys, it is imperative that this microstructure be quantified accurately in order to predict the mechanical behavior of the alloy. Microstructural information such as precipitate size, spacing, and volume fraction can be readily obtained *via* SAS, provided that information about the shape and type of the precipitates is known.^[2-5] SAS data are often used to show the characteristic rate law for the average precipitate radius.^[6-8] For coarsening, the precipitate radii should evolve with $t^{1/3}$ dependence under steady-state conditions, as theorized by Lifshitz, Slyozov, and Wagner (LSW theory);^[9,10] however, different rate laws have been obtained for rare cases in superalloys where simultaneous nucleation, growth, and coarsening occur or dual precipitate phases are present.^[7,8] Classic articles by Ardell and Nicholson^[11,12] have shown that coarsening of the γ' phase in nickel alloys is in excellent agreement with LSW coarsening theory except in cases where large coherency strains are present at the interface. Once the evolution in the precipitate size distributions is determined, this can be related to other measurable properties such as electrical resistivity for nondestructive evaluation purposes.

Since in-service turbine engine components undergo complex heating and cooling cycles, it is expected that the precipitate size distributions will be affected in a complex manner. It would be ideal to have a nondestructive method that could track changes in the precipitate distributions so that the mechanical behavior could be predicted as a function of such heat treatments. In order to do this, we propose that we first need to establish correlations between the scattering spectra and

the precipitate populations in samples with controlled precipitate size distributions and establish the precipitation kinetics and microstructural evolution. The next step will be to correlate this controlled precipitate microstructure to nondestructive electrical resistivity measurements. Once the simpler correlations have been made, scattering spectra of more complex thermal exposure profiles will be collected.

Electrical measurements provide a practical method of nondestructive evaluation and have already been used in nickel-base superalloys and other precipitation-hardenable systems.^[13-18] The electrical resistivity of a material is affected by lattice imperfections, by initial composition, and by dissolved impurities.^[19] As γ' can be considered a local lattice imperfection of the γ matrix phase and its formation will also lead to changes in the composition of the γ phase, it is expected that γ' precipitation will affect the resistivity response in a complex manner. Indeed, such a complex behavior has been shown for γ' precipitation-hardened systems, whereby an initial increase in resistivity was followed by a slower decrease with aging time.^[13-15] Wilson and Pickering^[13] observed this behavior for an austenitic stainless steel and attributed the initial increase in resistivity to scattering from small zones. These zones caused a maximum scattering of conduction electrons when they reached a diameter of approximately 1 nm.^[13] White *et al.*^[14] described a resistivity behavior portraying “a quasi-exponential increase, followed by a relatively slow decrease” for γ' precipitation in the Nimonic PE16 alloy (Henry Wiggins and Co. Ltd., Hereford, UK). They concluded that small precipitates, between 1 and 2 nm, as well as dissolved precipitate phase solute atoms, were the dominant conduction electron scatterers, with larger precipitates showing negligible electron scattering ability.^[14] Whelchel *et al.*^[15] observed a similar resistivity behavior along with correlations to Vickers microhardness, for γ' precipitation in WASPALOY. For the conditions reported in that article, it was found that the maximum in resistivity occurred well before the maximum in hardness; however, a maximum in conductivity occurred at similar aging times to the maximum in hardness.^[15]

It has also been shown that the γ' volume fraction in superalloys can be obtained as a function of temperature *via* electrical resistivity measurements.^[20] Obtaining quantitative microstructural information from electrical resistivity measurements on superalloys is an important first step toward using the electrical response as a nondestructive test of gas turbine engine components. An understanding of the precipitate microstructure's simultaneous effects on the electrical and mechanical behavior is necessary to create a link between the electrical properties and the mechanical properties in superalloy systems. Creation of a three-way correlation between the precipitate microstructure, electrical properties, and mechanical properties would render the electrical property measurement as an invaluable nondestructive technique for monitoring these alloys during service.

This is the second article in a series of investigations designed to identify methods of correlating the γ' precipitate population to the measured electrical resistivity. In the first article in this series,^[18] it was shown that

solution treatment temperatures, along with varying matrix grain size, had little effect on the γ' precipitation kinetics in WASPALOY. Instead, the aging treatment, specifically the aging temperature, 1052 K (779 °C) vs 1069 K (796 °C), was the dominant factor controlling the kinetics. A figure of merit of electron scattering was proposed by Kelekanjeri *et al.*,^[18] which related the measured electrical resistivity to the average precipitate radius and volume fraction of the precipitate phases.

In this article, the effect of varying the aging temperature on the microstructural evolution in WASPALOY will be evaluated for samples given a common supersolvus solution treatment followed by aging over a wider range of subsolvus temperatures than previously reported. A modified figure of merit for conduction electron scattering will be proposed, which will account for changes in the impurity content of the matrix phase due to precipitation of γ' , in addition to the precipitate size and volume fraction previously proposed.^[18]

II. PROCEDURE

A. Material and Heat Treatments

The materials examined were 13-mm-diameter bars of industrial grade WASPALOY obtained from Fry Steel. Three bars were solution treated at 1418 K (1145 °C) for 4 hours using a Carbolite model CDF 12/65/500 horizontal tube furnace (Carbolite, Watertown, WI) under an inert argon atmosphere. These bars were subsequently quenched in a ~5 wt pct NaCl and water solution heated to ~323 K (50 °C).

The solution-treated bars were subsequently aged at temperatures of 998 K, 1073 K, and 1148 K (725 °C, 800 °C, and 875 °C) for times ranging from 0.5 to 263.5 hours with a heating rate of 3.3 K/min (3.3 °C/min) during the heating cycle. Throughout the aging times described, intermediate quenching steps, and sampling for subsequent ultra small angle X-ray scattering (USAXS), microscopy, and electrical resistivity testing, were undertaken. Samples with thicknesses of approximately 2 mm were sectioned from the bars after each heat treatment (including solution treatment) in order to carry out the necessary microstructural characterization described previously. Following each sampling, the bars underwent further reheating, aging, and sampling steps, resulting in one extra reheating step for every subsequent aging time.

B. Microscopy

Microscopy specimens were ground with 400 US grit grinding papers followed by polishing with 9 and 3 μ m diamond suspensions. Further polishing was carried out *via* a suspension of four parts of 0.05- μ m colloidal silica plus one part of 30 pct H₂O₂, followed by a suspension of 0.05- μ m colloidal alumina. A preferential γ - γ' etchant was used to observe γ - γ' contrast. This etchant was comprised of 10 mL each of HCl, HNO₃, H₂O, and 0.3 g of molybdic acid reagent. A LEO 1530 scanning electron microscope was used to obtain microstructural images and energy dispersive spectroscopy (EDS)

measurements of the γ phase in equilibrium with the γ' phase.

C. Ultra Small Angle X-Ray Scattering

1. USAXS specimen preparation

USAXS specimens with approximate dimensions of 5×5 mm were ground *via* a series of 240, 400, 800, and 1200 US grit grinding papers *via* a Gatan disc grinder (Gatan, Inc., Pleasanton, CA) until final specimen thicknesses of approximately 10 to 20 μm were obtained. Specimen thicknesses in this range were necessary for the USAXS experiments due to the high X-ray absorption of Ni, which hinders the transmission of the X-ray beam.

2. USAXS measurements

USAXS experiments were conducted at the 32 ID beam line at the Advanced Photon Source at Argonne National Laboratory.^[21] The specimens were measured multiple times, and the statistical average and standard deviations of the microstructural information obtained from modeling the USAXS data are presented here. The USAXS measurements were performed with 11.9 keV X-rays. Intensity values were obtained for a Q range of approximately 10^{-4} to 1 \AA^{-1} . However, the Q range of interest for scattering from γ' precipitates was approximately 10^{-3} to 0.1 \AA^{-1} , as it has already been shown from the previous article in this series,^[18] and it is this Q range that is reported here.

3. Modeling of USAXS data

All data reduction and modeling were conducted through programs created *via* the Igor Pro software from

Wavemetrics, Inc. (Lake Oswego, Oregon). Data reduction was carried out *via* the Indra 2 package,^[22] whereas data modeling was carried out *via* the Irena 2 package.^[23] During data reduction, a blank scan was subtracted from the raw scattering data to yield slit smeared USAXS data. The absorption coefficient at the respective experimental energies was calculated using the WASPALOY composition quoted by Fry Steel. An approximate composition for the WASPALOY samples, which ignores trace elements, is as follows (in at. pct): Ni56.1, Cr21.2, Co12.3, Ti3.6, Al2.7, Mo2.5, and Fe1.3.

The absorption coefficient was used to calculate the specimen thicknesses from transmission data. These thicknesses were used to convert the slit-smeared data to absolute intensities.

Dilute scattering was assumed in all cases. In Eqs. [1] and [2], $F(Q)$ is the form factor for spherical scatterers, and $I(Q)$ is the expected intensity due to scattering from N particles of a single radius, r , in a specimen volume V .

$$F(Q) = \frac{3[\sin(Qr) - Qr \cos(Qr)]}{(Qr)^3} \quad [1]$$

$$I(Q) = \frac{N}{V} (\Delta\rho)^2 V_p^2 |F(Q)|^2 \quad [2]$$

The particle volume, V_p , was assumed to be the volume of a sphere of radius r . This assumption is correct since the γ' precipitates have been shown to be spherical (Figures 1 and 2 and References 16 and 17). The scattering contrast between the matrix and precipitates, $\Delta\rho^2$, was calculated using the composition of the

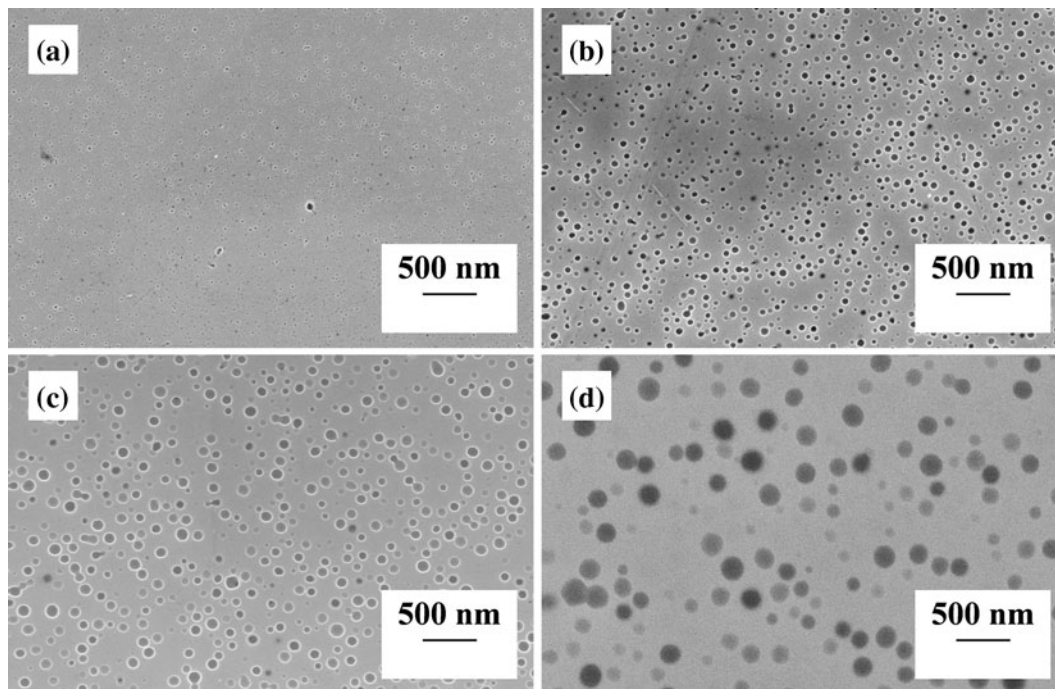


Fig. 1—SEM images of microstructural evolution upon aging at 1148 K (875 °C) for aging times of (a) 0.5 h, (b) 3.5 h, (c) 8.5 h, and (d) 263.5 h.

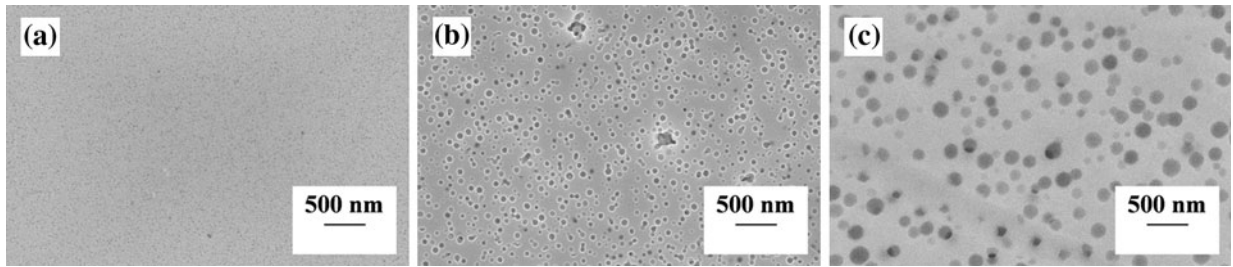


Fig. 2—SEM images of microstructural evolution upon aging for 163.5 h at aging temperatures of (a) 998 K (725 °C), (b) 1073 K (800 °C), and (c) 1148 K (875 °C).

matrix obtained from EDS measurements for specimens exposed to a preferential γ' etchant (given nominally as $\text{Ni}_{0.607}\text{Cr}_{0.2304}\text{Co}_{0.135}\text{Mo}_{0.028}$). The composition of the precipitate phase was assumed to be $\text{Ni}_3\text{Ti}_{0.5}\text{Al}_{0.5}$, since the chemical formula for γ' in Waspaloy is $\text{Ni}_3(\text{Al}, \text{Ti})$. The USAXS data were modeled with a volume distribution of precipitate sizes using equations described in detail by Ilavsky and Jemian^[23] and involve summing the parameters in Eq. [2] over this distribution. These equations were used to model the USAXS spectra over the relevant Q range for precipitate scattering.

Initial modeling was carried out *via* the Sizes routine within the Irena 2 package,^[23–25] assuming spherical scatterers for the γ' precipitates. This modeling yielded the particle size distributions, where no assumptions as to the size distribution type were required. The Sizes routine operates by assigning different scatterer sizes to appropriate radial bins, which does not involve fitting to a particular distribution type. The size distribution data from the Sizes routine was used as initial guesses for further modeling *via* the Modeling I routine,^[23] again assuming spherical scatterers. The Modeling I routine requires initial guesses as to the distribution type, average size, and volume fraction of scatterers. For these initial guesses, either a Gaussian or log normal size distribution was used along with the average size and volume fraction obtained *via* the Sizes routine. Gaussian and log normal curves were used since they resulted in the best fit to the USAXS data. The precipitate size distributions obtained from the Modeling I routine were used to calculate the average precipitate radius (r) and precipitate volume fraction (f_v) for each sample.

D. DC Four-Point Probe Resistivity Measurements

The experimental setup for resistivity measurements consisted of a Signatone model S301-6 probe station with a Signatone SP4-40045TFS four probe head, whereby the probe head had a spacing of 1 mm between each probe (Signatone Corporation, Gilroy, CA). A Keithley 6221 AC/DC current source and a Keithley 2182A nanovoltmeter were connected to the current and the voltage leads from the probe head, respectively (Keithley Instruments, Inc., Cleveland, OH). Resistance measurements were made at the center of each specimen along different diametric orientations with a source current of 50 mA. The resistance values were converted to resistivity values through the use of geometric correction factors

Table I. List of Multiple Specimens Used for Resistivity (R), USAXS (U), and Microscopy (M) Analysis of Waspaloy Specimens

Aging Time (h)	Aging Temperatures [K (°C)]	Specimens Tested
0.5	998, 1073, 1148 (725, 800, 875)	R, U, M
1.5	998, 1073, 1148 (725, 800, 875)	R, U, M
3.5	998, 1073, 1148 (725, 800, 875)	R, U, M
8.5	998, 1073, 1148 (725, 800, 875)	R, U, M
18.5	998, 1073, 1148 (725, 800, 875)	R, U, M
38.5	998, 1073, 1148 (725, 800, 875)	R, U, M
88.5	998, 1073, 1148 (725, 800, 875)	R, U, M
163.5	998, 1073, 1148 (725, 800, 875)	R, U, M
263.5	998, 1073, 1148 (725, 800, 875)	R, U, M

developed by Kelekanjeri and Gerhardt^[26] for four-point probe measurements along the diameter of the circular face of cylindrical specimens. The resistivity and the standard deviation in resistivity were derived from these correction factors, as described in detail by Kelekanjeri and Gerhardt^[17] in a different publication.

III. RESULTS

All of the samples that were heat treated and characterized for data reported in this publication are given in Table I.

A. Microscopy

The precipitate microstructures due to aging for various times at 1148 K (875 °C) are shown in Figure 1. The images show that the initial γ' phase is a small, closely spaced, spherical precipitate phase. The precipitates remain spherical throughout all aging times; however, as aging time progresses, the precipitates increase in size and spacing, as would be expected due to coarsening. It should be noted that similar microstructural evolution was observed for aging at 998 K and 1073 K (725 °C and 800 °C) albeit at a slower rate, and Figure 1 is meant to serve as a representative example for γ' microstructural evolution in these materials. The precipitate microstructures due to aging for 163.5 hours at 998 K, 1073 K, and 1148 K (725 °C, 800 °C, and 875 °C) are shown in Figure 2. The images again show spherical precipitate phases (as was observed in Figure 1); however, the

precipitate size increases dramatically with increasing temperature. This is as expected due to the progressively faster precipitation kinetics associated with increasing aging temperatures.^[27]

B. Ultra Small Angle X-Ray Scattering

1. USAXS spectra

The intensity vs scattering vector (Q) data acquired via USAXS for the 1148 K (875 °C) sample series are shown in Figure 3. The data for each sample have been shifted in intensity to enhance readability. Figure 3 contains data from only one aging series and is meant to act as a representative example for all of the experiments performed. The data show regions that appear to be linear for the log-log axes shown, but the intensity actually decreases with Q^{-n} dependence in each region, where n is a positive nonzero integer. These regions, known as Debye regions, are separated by inflection points and represent scattering from distinct scattering size populations. The Debye region in the low Q range (region I in Figure 3) is due to large (micron-sized) objects, which are not the subject of the present study. This Debye region is believed to result from scattering from the grain structure or from carbides present at the grain boundaries. In previous work,^[18] it has been shown that the precipitate kinetic behavior, which is the subject of the current study, is not a function of the γ matrix grain size. However, since the specimens were all given a common solution treatment, the grain size was essentially constant for every sample in this study ($\sim 85 \mu\text{m}$). Furthermore, the specimens appear to have few or no carbides. Therefore, the relevant scattering region for the present study is that attributed to γ' and has a Q range from approximately 0.001 to 0.1 \AA^{-1} . Thus, it is this Q range that was subsequently modeled. The primary precipitate phase scattering region is denoted by region II in Figure 3.

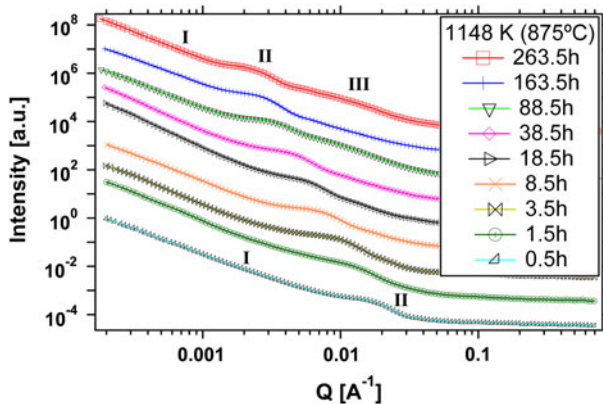


Fig. 3—Intensity vs Q plots for samples aged at 1148 K (875 °C). The data for each aging time have been shifted in intensity for easier viewing. Similar curves were obtained for samples aged at 998 K and 1073 K (725 °C and 800 °C). Regions I, II, and III represent large scattering objects, the primary precipitate phase, and the secondary precipitate phase, respectively.

Region II shifts to progressively lower Q values with increasing aging time. Since Q is inversely proportional to the actual size of the scattering object, the data show increasing precipitate size with aging, which corroborates the microstructural evolution noted from scanning electron microscopy (SEM) images (Figures 1 and 2). With increasing aging time, a third Debye region (region III in Figure 3) appears in the data at higher Q than that of the primary distribution, showing the formation of a smaller, secondary precipitate population. This is also corroborated by SEM images, as Figures 1 and 2 do exhibit smaller precipitates interspersed with the primary, large precipitates at longer aging times.

2. Microstructural information from USAXS

Subsequent modeling of the USAXS data yielded the precipitate size distributions (PSDs), average precipitate radii ($\langle r \rangle$), and average precipitate volume fractions ($\langle f_v \rangle$). Figure 4 shows an initial, primary γ' precipitate population (region II in Figure 3), which shifts to larger diameters with aging time for all temperatures. Eventually, a smaller, secondary precipitate population (region III in Figure 3) is observed for all temperatures, which is retained with further aging. The formation of the secondary precipitate population occurs at progressively lower aging times with increasing temperature.

The average over all USAXS experiments for the primary precipitate radii ($\langle r_p \rangle$) and secondary precipitate radii ($\langle r_s \rangle$) as a function of aging time and temperature are shown in Figure 5. The standard deviations shown for each point were calculated from averaging the precipitate radii obtained from two different scattering runs on the same samples. A clear progressive increase in $\langle r_p \rangle$ is seen with aging time. An increasing trend in $\langle r_s \rangle$ is also seen with aging time; however, there is not a progressive increase, as seen with $\langle r_p \rangle$, and the standard deviations are much higher for $\langle r_s \rangle$. It should be noted that the precipitate radii predicted from USAXS modeling are similar to the precipitate radii seen in Figures 1 and 2.

The average over all USAXS experiments for the primary volume fraction ($\langle f_{v,p} \rangle$), secondary volume fraction ($\langle f_{v,s} \rangle$), and total volume fraction ($\langle f_{v,t} \rangle$) as a function of aging time and temperature are shown in Figure 6. The $\langle f_{v,p} \rangle$ plot reaches a peak, followed by a decreasing trend in the case of the 998 K and 1148 K (725 °C and 875 °C) samples, with peaks occurring at 18.5 and 1.5 hours, respectively. At 1073 K (800 °C), $\langle f_{v,p} \rangle$ decreases throughout all aging times. In contrast, the $\langle f_{v,s} \rangle$ plot shows a fluctuating behavior with aging time for all temperatures, and the data points associated with varying temperature are all within their own standard deviations for each aging time. The average total volume fraction, $\langle f_{v,t} \rangle$, displays an initial peak, but in contrast to the average primary volume fraction, $\langle f_{v,p} \rangle$, a broad peak appears in the 1073 K (800 °C) specimen set. The peak locations occur at 18.5, 8.5, and 1.5 hours for aging at 998 K, 1073 K, and 1148 K (725 °C, 800 °C, and 875 °C) respectively. After the initial peak, $\langle f_{v,t} \rangle$ displays the fluctuating behavior noted from $\langle f_{v,s} \rangle$, with an additional peak visible at 88.5 hours for aging at 1073 K and 1148 K (800 °C and 875 °C).

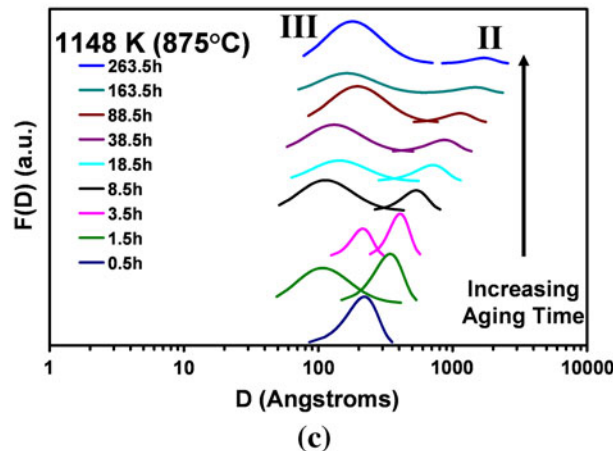
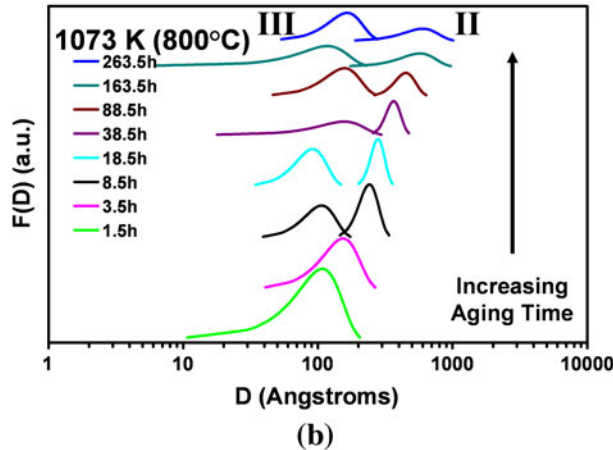
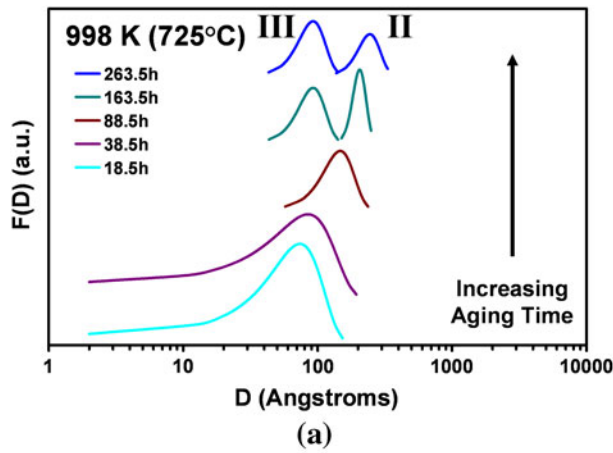


Fig. 4—Precipitate size distributions for samples aged at (a) 998 K (725 °C), (b) 1073 K (800 °C), and (c) 1148 K (875 °C). The roman numerals indicate the scattering region from Fig. 3 associated with each distribution.

3. Coarsening behavior

The coarsening behavior of the primary γ' precipitates is presented in Figure 7 as a plot of $\langle r_p \rangle^3$ vs aging time. Figure 7 is included solely to prove that the precipitates are in the coarsening regime for the aging treatments used. No attempt has been made to obtain activation energies from these data, and the coarsening behavior is only presented in order to show the characteristic rate

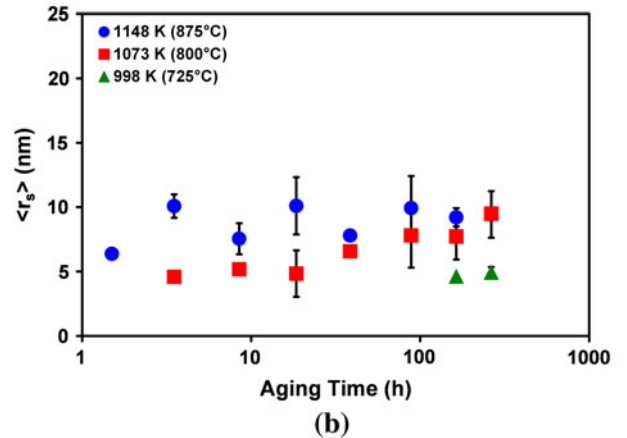
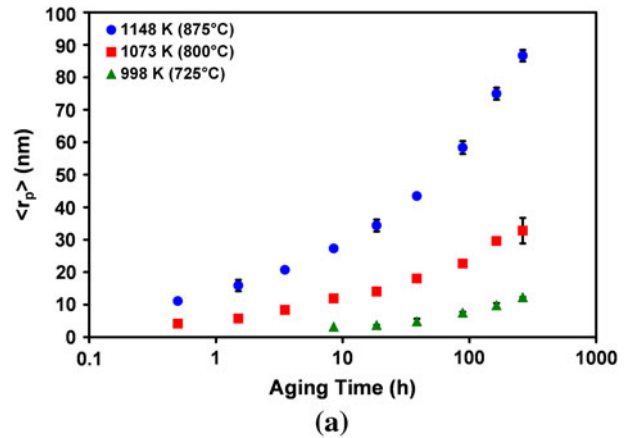


Fig. 5—Average precipitate radii for the (a) primary and (b) secondary γ' precipitate populations as a function of aging time.

law for the particle radii. The data were fit with a linear least-squares trend line, showing the $t^{1/3}$ dependence of $\langle r_p \rangle$ for γ' coarsening. The inset in Figure 7 better displays the vastly increasing slopes with increasing aging temperature, where the slopes of the linear fits represent the coarsening rate constants at the respective temperatures.

It should be noted that the coarsening data for aging at 998 K (725 °C) have the worst linear fit ($R^2 = 0.97$) of the three aging times presented. A plot of the natural logarithm of $\langle r_p \rangle$ vs the natural logarithm of the aging time at 998 K (725 °C) revealed that $\langle r_p \rangle$ actually increases with a $t^{0.4}$ temporal power law, as opposed to the normal $t^{1/3}$ dependence from diffusion-controlled coarsening; however, similar plots for aging at 1073 K and 1148 K (800 °C and 875 °C) confirmed that $\langle r_p \rangle$ obeyed a $t^{1/3}$ temporal power law throughout all aging times presented in this article. No $t^{1/3}$ dependence was noted for the $\langle r_s \rangle$ data. This is a similar observation to that made by Rogante and Lebedev,^[8] wherein the smaller precipitate size distribution portrayed a different growth rate than that of the larger precipitate size distribution.

C. Electrical Resistivity Data

The electrical resistivity data are shown in Figure 8, where the data points shown at 0.01 hours represent the

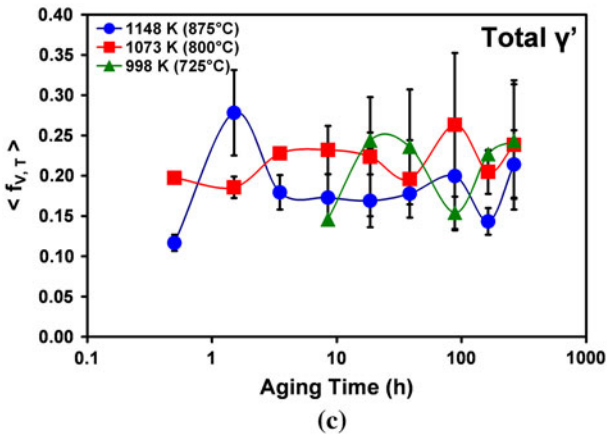
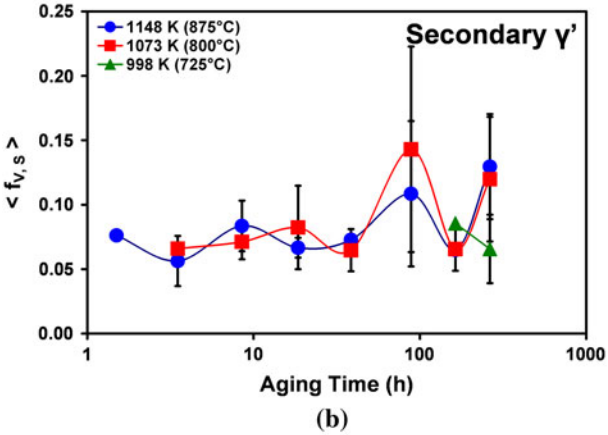
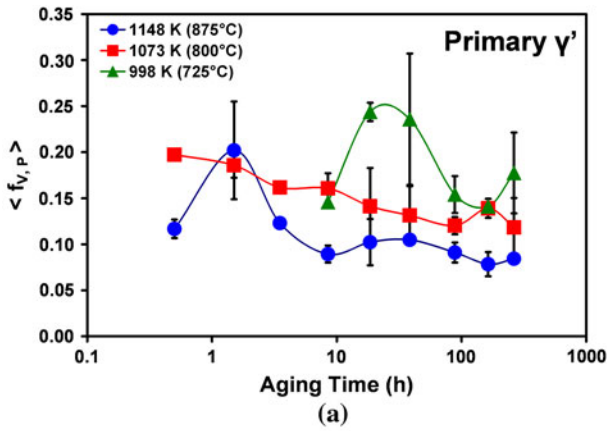


Fig. 6—Volume fractions for (a) primary, (b) secondary, and (c) total precipitate populations.

solution-treated samples. The resistivity displays an initial increasing trend with aging time for the samples aged at 998 K and 1073 K (725 °C and 800 °C), but the samples aged at 1148 K (875 °C) did not display such an increase in resistivity. Aging at 1148 K (875 °C) resulted in a continuous decrease in resistivity with aging time. This is most likely due to the rapid precipitation kinetics at 1148 K (875 °C); consequently, there was not enough time available to sample the material such that an increasing resistivity region could be detected. As noted for aging at 1148 K (875 °C), the resistivity also progressively decreased after 1.5 and 0.5 hours of aging

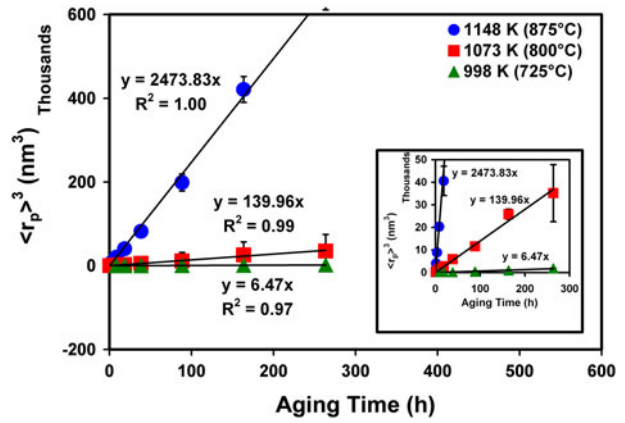


Fig. 7—Coarsening plots with least-squares linear fits showing $t^{1/3}$ dependence of the average primary γ' precipitate radii with aging.

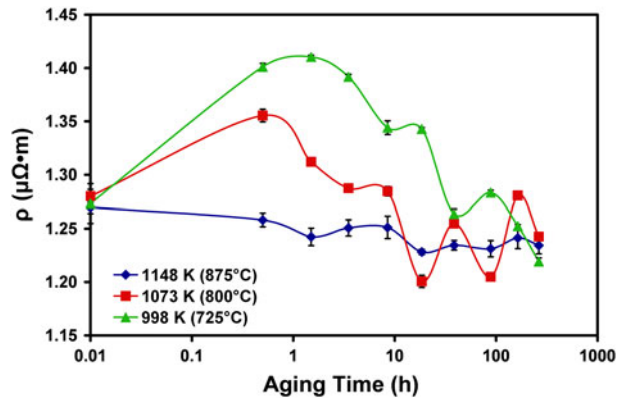


Fig. 8—Electrical resistivity data for aging at 998 K, 1073 K, and 1148 K (725 °C, 800 °C, and 875 °C). The 1148 K (875 °C) data was published as conductivity in an earlier publication.^[13]

at 998 K and 1073 K (725 °C and 800 °C), respectively. Prolonged aging resulted in a fluctuating resistivity behavior similar to the fluctuating behavior seen for the secondary precipitate volume fraction. The initial increase followed by the slower decrease in resistivity is as noted previously for several precipitation-hardened materials.^[13–15]

IV. DISCUSSION

A. Microstructural Information from USAXS

1. Primary precipitate population

The primary precipitate size distributions shown in Figure 4 show a progressive shift to larger diameters with aging time, which is also shown by the progressive increase in the average primary precipitate radii, $\langle r_p \rangle$, in Figure 5. The precipitates were determined to be in the coarsening stage throughout all aging times at 1073 K and 1148 K (800 °C and 875 °C), as evidenced by the expected $t^{1/3}$ temporal power law for $\langle r_p \rangle$ associated with diffusion-controlled coarsening. Aging at 998 K (725 °C) resulted in a $t^{0.4}$ temporal power law for $\langle r_p \rangle$, which is

most likely due to a mixed mode of growth and coarsening.

The average primary γ' volume fraction, $\langle f_{v,p} \rangle$, seen in Figure 6, reaches a peak, followed by a decreasing trend except for the samples aged at 1073 K (800 °C). The $\langle f_{v,p} \rangle$ data for the samples aged at 1073 K (800 °C) appear to decrease throughout all aging times; however, a high standard deviation is noted for the sample aged for 1.5 hours, indicating a possible peak location. Further evidence for a peak comes from the fact that Kelekanjeri *et al.*^[18] noted a peak in the primary volume fraction occurring at 1.5 hours for similarly aged specimens at 1073 K (800 °C). However, these specimens were also exposed to a vacancy stabilization treatment in addition to the solution treatment and aging treatment. It is believed that the maxima in $\langle f_{v,p} \rangle$ indicate that the precipitates have reached their equilibrium volume fraction for the particular aging temperature. Further aging results in a decrease in $\langle f_{v,p} \rangle$. This is most likely due to smaller precipitates from the primary distribution joining with the secondary distribution. The maxima in $\langle f_{v,p} \rangle$ occur at decreasing volume fractions for increasing temperature. This is as expected due to the increasing solid solubility of precipitate phase solute in the matrix phase at higher temperature.

B. Secondary Precipitate Population

The PSDs shown in Figure 4 show a progression from a unimodal to a bimodal distribution with increasing aging time in all cases. The aging time required to engender the shift to a bimodal behavior decreases with increasing temperature, implying that the kinetics required to form the secondary precipitate distribution are faster at elevated temperatures. It is speculated that these secondary populations are a result of the multiple heating-up cycles used for the aging procedure. In this study, the samples were repeatedly exposed to low temperatures upon reheating at each aging step, during which the driving force for nucleation would be high. Upon further heating, any nuclei formed would be exposed to high enough temperatures for diffusion to occur, which could result in subsequent growth or coarsening of the secondary precipitate phase.

Figure 5 shows that $\langle r_s \rangle$ does not increase progressively with aging time, as does $\langle r_p \rangle$. It has also been noted that $\langle r_s \rangle$ does not display $t^{1/3}$ dependence, which would be expected for precipitate coarsening; however, $\langle r_s \rangle$ does progressively increase with temperature for a given aging time, suggesting that a thermally activated process is occurring. It is believed that the secondary precipitate population is undergoing more than one process during the consecutive heating cycles. The competing mechanisms of growth and coarsening could account for the complex kinetic behavior noted for the secondary precipitate population.

Unlike $\langle r_s \rangle$, the average secondary precipitate volume fraction, seen in Figure 6, does not display noticeable aging temperature dependence. At any given aging time, all the data points corresponding to the different aging

temperatures fall within the reported standard deviations.

C. Correlations between Microstructural Information and Electrical Measurements

1. Electrical resistivity data

The initial increase in resistivity noted for aging at 998 K and 1073 K (725 °C and 800 °C) can be attributed to the scattering effects of small precipitates. White *et al.*^[14] mentioned that small precipitates and solute atoms dissolved in the matrix are the major contributors to electrical resistivity at low aging times. Since the precipitates are very small at low aging times and the amount of solute in the matrix is also high, it is expected that the samples will display a high resistivity at low aging times.

The eventual decrease in resistivity noted for all aging temperatures can be partly attributed to coarsening, whereby the γ' evolves from small, finely spaced precipitates into larger, widely spaced precipitates, effectively increasing the electron mean free path through the microstructure. Another factor affecting this decreasing resistivity range will be the purity of the matrix phase. As already described, solute atoms dissolved in the matrix phase can cause significant conduction electron scattering. As aging time increases, the volume fraction of precipitates also increases, effectively removing precipitate forming solute elements from solution in the matrix phase, and therefore decreasing the resistivity of the matrix phase.

Prolonged aging (>8.5 hours) resulted in a fluctuating resistivity behavior similar to the fluctuating behavior seen for the secondary precipitate volume fraction. This correlation suggests that the electron scattering behavior of the secondary precipitates is the dominant scattering force at long aging times. The fluctuating resistivity behavior occurs in a region where the primary precipitate volume fraction has leveled off, and due to the long aging times, the nearest neighbor distance for the primary precipitates is quite large. The stable volume fraction and large separation distance imply that electron scattering from the primary precipitate phase will not change significantly for this aging time region. In contrast, the secondary precipitates have a fluctuating volume fraction and are finely spaced, which would result in a widely varying electron scattering behavior. This expected change in electron scattering explains the similarity between the resistivity and the secondary volume fraction at longer aging times.

2. Geometrical effects of precipitates on electron scattering

Kelekanjeri *et al.*^[18] previously proposed a figure of merit of scattering, η , which correlates microstructural data obtained from USAXS derived precipitate size distributions to electrical resistivity data. The assumptions for η are as follows:

- (1) The degree of electron scattering is assumed to be directly proportional to the total scattering area per unit volume and inversely proportional to the average nearest neighbor distance.

- (2) The scatterers are assumed to be spherical.
- (3) The average nearest neighbor distance is assumed to be that of a random distribution of point particles in an infinite volume.

The final result for the figure of merit of electron scattering proposed by Kelekanjeri *et al.*^[18] is given by Eq. [3]:

$$\eta = 3.33 \sum_i \frac{\langle f_{v,i} \rangle^{4/3}}{\langle r_i \rangle^2} \quad [3]$$

In Eq. [3], the summation is performed over each precipitate size distribution. Kelekanjeri *et al.*^[18] observed initial large values in η due to scattering from small precipitates followed by a large decrease to a small constant value due to increasing nearest neighbor distance.

3. Matrix composition effects on electron scattering

Kelekanjeri *et al.*^[18] mention that the formulation for η given by Eq. [3] shows a generic correlation to electrical resistivity in four different specimen sets, two aged at 1052 K (779 °C) and two aged at 1069 K (796 °C). However, it should be noted that Eq. [3] only accounts for electron scattering arising from geometrical effects of precipitates. The derivation is solely based on precipitate area and nearest neighbor distance, which would be accurate if the matrix composition remained constant throughout all aging times. However, the formation of the γ' precipitate phase involves preferentially removing precipitate forming elements (in our case, Ti and Al) from solution in the Ni-rich γ matrix phase. This would result in a purer matrix phase as precipitation of the γ' continues. From Matthiessen's rule, it is to be expected that this purer matrix phase would result in a lesser degree of electron scattering than the initial, solutionized matrix phase.

The overall resistivity trend with aging is due to different electron scattering mechanisms becoming dominant during different stages of the aging process. At low aging times, the fine γ' distribution and solid solution impurities are the dominant electron scatterers. During early stages of aging, the increase in resistivity over and above that due to solid solution impurities is attributed to scattering from the fine γ' distribution. With continued aging, coarsening of γ' occurs with simultaneous transfer of γ' forming elements from the matrix phase, thereby lowering the impurity concentration of the matrix phase. The scattering effect from solid solution impurities, however, is not captured in the formulation of η , as pointed out by Kelekanjeri *et al.*^[18] At longer aging times, the γ' interparticle spacing becomes so large that the scattering contribution to resistivity from γ' precipitates is minimal.

In this article, an additional term involving matrix composition effects (η_c) is proposed, which can be added to the previous formulation for η given by Eq. [3]. From this point onward, the formulation for η given by Eq. [3] shall be referred to as η_g , as this involves only the geometrical effects of precipitates on scattering. Adding the compositional term, η_c , to the geometrical term, η_g ,

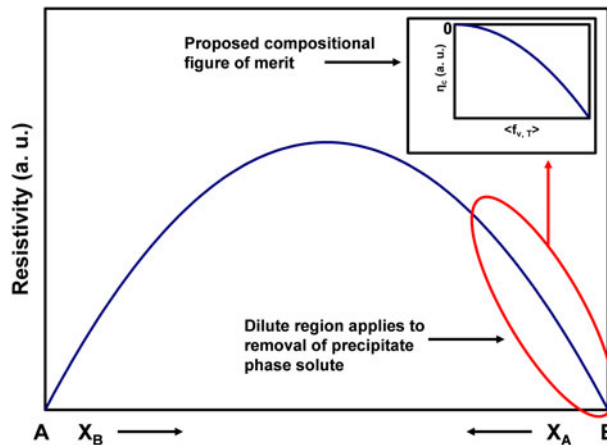


Fig. 9—Schematic of resistivity behavior for a hypothetical binary alloy A-B in complete solid solution. The inset displays the behavior for the proposed figure of merit of scattering due to matrix composition effects (η_c).

should give a new figure of merit of electron scattering, which incorporates both electron scattering effects, those of γ' precipitates and those of solute impurities in the Ni-rich matrix. This new figure of merit shall be designated as η' :

$$\eta' = \eta_g + \eta_c \quad [4]$$

Let us now discuss how we can quantify the effect of the changing matrix composition as γ' precipitation proceeds. The expected electrical response of a hypothetical binary A-B alloy in complete solid solution is depicted schematically in Figure 9. Matthiessen's rule states that an alloy solid solution will have lower values of resistivity as the composition moves toward pure component A or pure component B, with a maximum occurring somewhere in between. If we let the highest point of the circled region represent the Ni-rich matrix composition (with all solutes in solution), it follows that when precipitation of γ' occurs, then the resistivity of the matrix will decrease, as shown. Since η_c is meant to model the resistivity of the matrix phase due to compositional changes, one would expect η_c to have a shape similar to that shown in Figure 9. However, in the case of η_c , the variable of interest is the total volume fraction of γ' precipitates, $f_{v,T}$, which cause the change in resistivity, as seen by the inset of Figure 9. It should also be noted that increasing the volume fraction of precipitates removes precipitate forming elements from solution in the matrix phase, effectively reducing the composition of these elements in the matrix while maintaining the same solute content for all the other impurities that do not participate in the γ' precipitation. The inset of Figure 9 assumes that any γ' precipitation results in a more conductive matrix phase, and this is what controls η_c . This does not necessarily mean that η' should always decrease with increasing $f_{v,T}$, since η_g will be very high at low aging times (when the total volume fraction $f_{v,T}$ is low), due to the small size of the initially formed γ' precipitates. Increases in the γ' volume

fraction result in decreasing η_c , as the matrix is expected to become more conductive as γ' forming solute is removed from the solution in the matrix phase. It is therefore proposed that η_c can be modeled as a second-order polynomial, as shown subsequently:

$$\eta_c = -C\langle f_{v,T} \rangle^2 \quad [5]$$

In Eq. [5], C is a positive constant, giving η_c a negative curvature, as proposed in Figure 9. Combining Eqs. [3] through [5] yields

$$\eta' = \eta_g + \eta_c = 3.33 \sum_i \frac{\langle f_{v,i} \rangle^{4/3}}{\langle r_i \rangle^2} - C\langle f_{v,T} \rangle^2 \quad [6]$$

In Eq. [6], the first term (η_g) acts to increase electron scattering and is dominant for small, closely spaced precipitates, as is expected at low aging times. The second term (η_c) acts to decrease electron scattering and is dominant for high volume fractions of precipitates, as is expected at long aging times. We are proposing that some form of Eq. [6] can be used to model the complex behavior noted in the measured resistivity for precipitation hardenable systems, yielding a correlation between the strengthening precipitate microstructure and the electrical response.

4. Figure of merit modeling for WASPALOY

The microstructural information obtained from USAXS ($\langle r_p \rangle$, $\langle r_s \rangle$, $f_{v,P}$, $f_{v,S}$, and $f_{v,T}$) was used along with Eq. [6] to calculate η' for the aged WASPALOY specimens. All variables in Eq. [6] are microstructural variables except for the constant, C . This constant was iteratively varied in order to give the best fit of η' to the resistivity data. The empirical trends in the electrical resistivity, η_g , and η' as a function of aging time are shown in Figure 10. It can be seen that the improved figure of merit, η' , shows empirical correlations between the measured electrical response over a wider range of aging times and temperatures than for the geometrical figure of merit, η_g .

The figure of merit of scattering, η' , being proposed here is a simplified model of electrical behavior, whereby electron scattering from precipitates and matrix purity effects on electron scattering are considered to be the only two factors affecting the electrical response. It is possible that a more complex model is needed involving more microstructural parameters than those discussed here. Crystalline defects such as vacancy concentration, carbide concentration, or dislocation density may also play a role in the electrical scattering behavior of precipitation-hardened materials. Since the constant, C , in Eq. [6] was solved for in an iterative fashion, this makes η_c an empirical equation. A more accurate model might involve fitting a curve to actual resistivity data for several solutionized bulk WASPALOY compositions. These data could be used to solve for the constant, C , directly. Unfortunately, this procedure is not practical, as the range of available WASPALOY compositions is quite small compared to the matrix compositional changes expected due to precipitation.

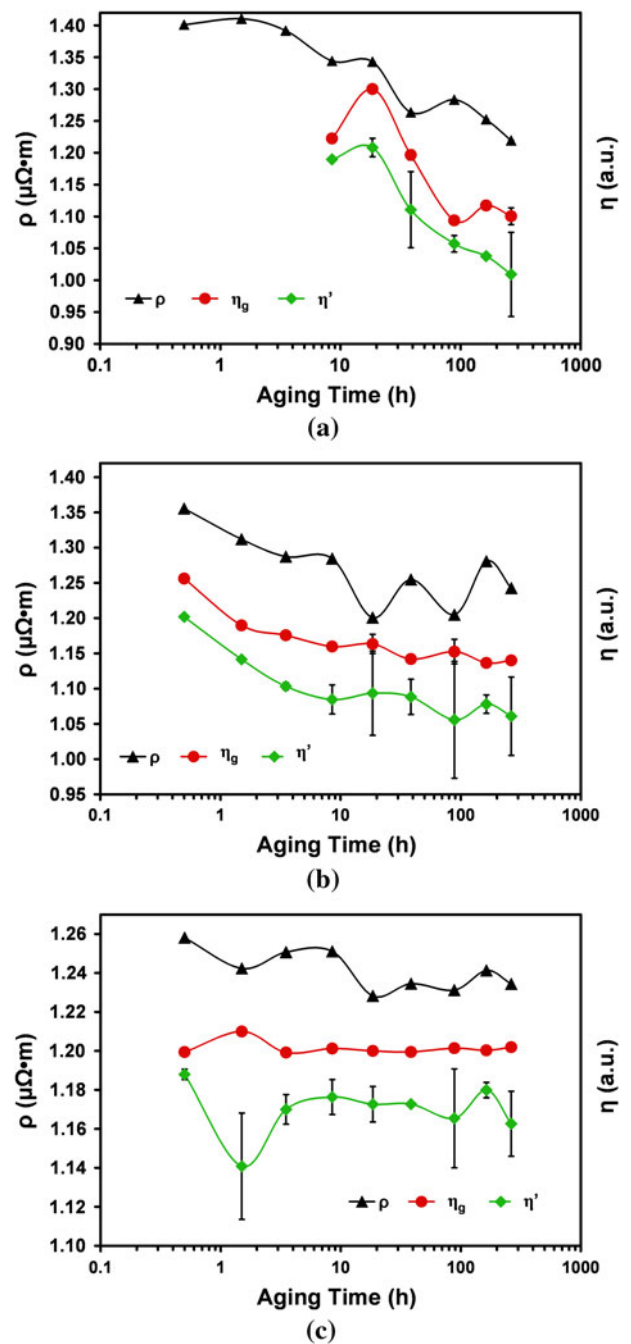


Fig. 10—Comparison of resistivity to geometric (η_g) and modified (η') figures of merit of electron scattering as a function of aging time at (a) 998 K (725 °C), (b) 1073 K (800 °C), and (c) 1148 K (875 °C). Note the similarity between the resistivity curve and the modified figure of merit.

The proposed figure of merit of electron scattering could be further improved to give a direct link between the evolving γ' precipitate microstructure and the evolving electrical resistivity behavior in WASPALOY. This will require inclusion of the effects of strain in the material due to matrix-precipitate incoherency, as well as improving the modeled matrix composition effects on resistivity due to each alloying element individually. Establishing a more accurate model would lead to the

development of master curves that relate η' , a measure of the precipitate microstructure, to the resistivity response. Future work will involve refining the model, as described previously, followed by relating the proposed figure of merit to the mechanical properties in WASPALOY. Once this three-way correlation is made, then the proposed figure of merit can be used for monitoring the mechanical properties in age-hardened materials operating under cyclic thermal exposure. The implications of such a correlation would be that η' and resistivity could be used as a nondestructive testing method for age-hardened materials, which would ultimately result in better lifetime prediction for gas turbine engine components.

V. CONCLUSIONS

USAXS has proven to be a reliable method for microstructural characterization of precipitation-hardened WASPALOY. The USAXS analysis shows an initial unimodal γ' precipitate size distribution, which progresses to a bimodal distribution with continued aging. The primary precipitate radii increase with $t^{1/3}$ dependence for aging at 1073 K and 1148 K (800 °C and 875 °C), as expected from coarsening; however, the primary precipitate radii increase with $t^{0.4}$ dependence for aging at 998 K (725 °C), indicating mixed growth and coarsening. For the secondary precipitate population, the radii increase in a more complex fashion. Moreover, the secondary precipitate volume fractions display a fluctuating behavior throughout all aging times, with no apparent dependence on aging temperature. It is believed that the primary precipitate size distribution is controlled by the soak time at each particular aging temperature, whereas the smaller, secondary precipitate size distribution is the result of the cyclic heating schedule used.

A figure of merit of electron scattering has been proposed, which takes into account both the effects of scattering from precipitates and the effects of varying matrix purity due to precipitation. The figure of merit displays empirical similarities to the measured electrical resistivity of the WASPALOY samples over a wider range of aging times and temperatures than modeling without matrix purity effects. The proposed figure of merit shows promise for correlating the electrical response of age-hardened WASPALOY to the underlying precipitate microstructure.

ACKNOWLEDGMENTS

The authors acknowledge the funding for this work provided by the United States Department of Energy

under Grant No. DE-FG 02-03-ER 46035. Use of the Advanced Photon Source was supported by the United States Department of Energy, Office of Science, Office of Basic Energy Sciences, under Contract No. DE-AC02-06CH11357.

REFERENCES

1. R.C. Reed: *The Superalloys*, Cambridge University Press, New York, NY, 2006, pp. 73–81.
2. P. Staron, U. Christoph, F. Appel, and H. Clemens: *Appl. Phys. A*, 2002, vol. 74, pp. 1163–65.
3. M. Sundararaman, W. Chen, R.P. Wahi, A. Wiedenmann, W. Wagner, and W. Petry: *Acta Metall. Mater.*, 1992, Ser. 5, vol. 40, pp. 1023–28.
4. D. Mukherji, D. Del Genovese, P. Strunz, R. Gilles, A. Wiedenmann, and J.J. Rosler: *J. Phys. Condens. Matter*, 2008, vol. 20, pp. 104220–28.
5. J. Zrník, P. Strunz, P. Hornak, V. Vrchovinsky, and A. Wiedenmann: *Appl. Phys. A*, 2002, vol. 74, pp. 1155–57.
6. S. Zhao, X. Xie, G.D. Smith, and S.J. Patel: *Mater. Lett.*, 2004, vol. 58, pp. 1784–87.
7. F. Bley, F. Livet, O. Lyon, H. Okuda, and J.P. Simon: *J. Appl. Crystallogr.*, 1997, vol. 30, pp. 914–17.
8. M. Rogante and V.T. Lebedev: *Mater. Des.*, 2008, vol. 29, pp. 1060–65.
9. I.M. Lifshitz and V.V. Slyozov: *Phys. Chem. Solids*, 1961, Ser. 35, vol. 19, pp. 35–50.
10. C. Wagner: *Z. Electrochem.*, 1961, vol. 65, pp. 581–91.
11. A.J. Ardell and R.B. Nicholson: *Phys. Chem. Solids*, 1966, vol. 27, pp. 1793–804.
12. A.J. Ardell and R.B. Nicholson: *Acta Metall.*, 1966, vol. 14, pp. 1295–309.
13. F.G. Wilson and F.B. Pickering: *Acta Metall.*, 1968, vol. 16, pp. 115–31.
14. R.J. White, S.B. Fisher, K.M. Miller, and G.A. Swallow: *J. Nucl. Mater.*, 1974, vol. 52, pp. 51–58.
15. R.L. Whelchel, V.S.K.G. Kelekanjeri, and R.A. Gerhardt: *Int. Heat Treat. Surf. Eng.*, 2009, Ser. 1–2, vol. 3, pp. 35–39.
16. V.S.K.G. Kelekanjeri and R.A. Gerhardt: *Adv. Mater. Res.*, 2007, vols. 15–17, pp. 876–81.
17. V.S.K.G. Kelekanjeri and R.A. Gerhardt: *Acta Mater.*, 2009, Ser. 2, vol. 57, pp. 616–27.
18. V.S.K.G. Kelekanjeri, L. Moss, R.A. Gerhardt, and J. Ilavsky: *Acta Mater.*, 2009, Ser. 16, vol. 57, pp. 4658–70.
19. Safa O. Kasap: *Principles of Electronic Materials and Devices*, 3rd ed., McGraw-Hill, New York, NY, 2006, pp. 125–39.
20. B. Roebuck, D. Cox, and R. Reed: *Scripta Mater.*, 2001, vol. 44, pp. 917–21.
21. J. Ilavsky, P.R. Jemian, A.J. Allen, F. Zhang, L.E. Levine, and G.G. Long: *J. Appl. Crystallogr.*, 2009, vol. 42, pp. 469–79.
22. J. Ilavsky, A.J. Allen, G.G. Long, and P.R. Jemian: *Rev. Sci. Instrum.*, 2002, vol. 73, pp. 1660–62.
23. J. Ilavsky and P.R. Jemian: *J. Appl. Crystallogr.*, 2009, vol. 42, pp. 347–53.
24. J.A. Potton, G.J. Daniell, and B.D. Rainford: *J. Appl. Crystallogr.*, 1988, vol. 21, pp. 663–68.
25. P. Jemian, G. Long, F. Lofaj, and S. Wiederhorn: *Mater. Res. Soc. Symp. Proc.*, 2000, vol. 590, pp. 131–36.
26. V.S.K.G. Kelekanjeri and R.A. Gerhardt: *Meas. Sci. Technol.*, 2008, ser. 2, vol. 19., pp. 025701–12.
27. D.A. Porter and K.E. Easterling: *Phase Transformations in Metals and Alloys*, 2nd ed., Taylor and Francis Group, Boca Raton, FL, 2004, pp. 291–317.